

Attacking Important Pixels for Anchor-free Detectors

Yunxu Xie*, Shu Hu*, Xin Wang[‡], *Senior Member, IEEE*,
Quanyu Liao, Bin Zhu, Xi Wu[‡], Siwei Lyu *Fellow, IEEE*

Abstract—Deep neural networks have been demonstrated to be vulnerable to adversarial attacks: subtle perturbation can completely change the prediction result. Existing adversarial attacks on object detection focus on attacking anchor-based detectors, which may not work well for anchor-free detectors. In this paper, we propose the first adversarial attack dedicated to anchor-free detectors. It is a category-wise attack that attacks important pixels of all instances of a category simultaneously. Our attack manifests in two forms, sparse category-wise attack (SCA) and dense category-wise attack (DCA), that minimize the L_0 and L_∞ norm-based perturbations, respectively. For DCA, we present three variants, DCA-G, DCA-L, and DCA-S, that select a global region, a local region, and a semantic region, respectively, to attack. Our experiments on large-scale benchmark datasets including PascalVOC, MS-COCO, and MS-COCO Keypoints indicate that our proposed methods achieve state-of-the-art attack performance and transferability on both object detection and human pose estimation tasks.

Index Terms—Adversarial Attack, Object Detection, Human Pose Estimation, Category-wise Attack, Anchor-free Detector

I. INTRODUCTION

THE development of deep neural networks (DNNs) [1]–[5] enables researchers to achieve unprecedented high performance on various computer vision tasks. However, DNN models are vulnerable to adversarial examples: intentionally crafted subtle disturbance on a clean image makes a DNN model predict incorrectly [6], [6]–[16]. As a typical type DNNs, convolutional neural networks (CNNs) achieve state-of-the-art (SOTA) performance on classification, objection detection, segmentation, and other computer vision tasks but also suffer from adversarial examples [17], [18]. Studies on generating adversarial examples have attracted increasing attention because they help identify vulnerabilities of trained DNN models before they are launched in services.

Object detection is essential in many vision tasks like instance segmentation, pose estimation, and action recognition. Existing object detectors can be classified into two groups according to the way they locate objects: anchor-based [19], [21]–[25] and anchor-free detectors [20], [26]–[29]. An anchor-based detector first determines many preset anchors on the image and then refines their coordinates and

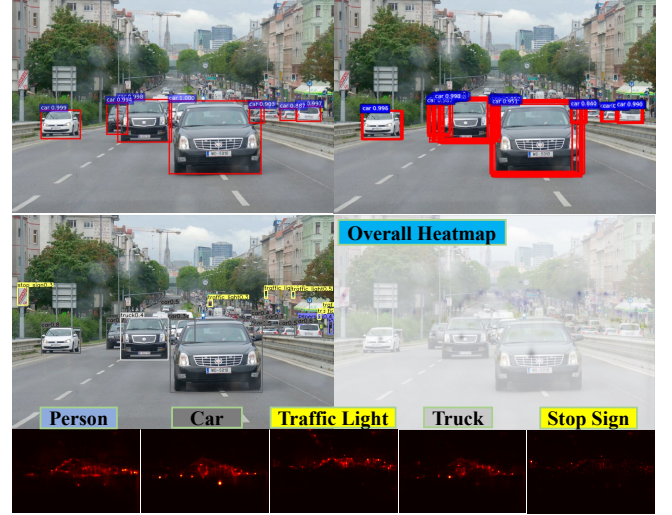


Fig. 1: **First row:** The detected results (left) and the proposals (right) of Faster-RCNN [19]. **Second row:** The detected results (left) and the overall heatmap (right) of CenterNet [20]. **Third row:** Selected target pixels (red) that will be attacked by our methods.

predicts their categories before outputting final detection results (see the first row in Fig. 1). An anchor-free detector finds objects without using preset anchors: it detects keypoints of objects and then bounds their spatial extent (see Fig. 1 second row). There are many works on adversarial attacks against anchor-based detectors, such as DAG [13] and UEA [12]. However, to the best of our knowledge, there is no published work except our published conference papers [30], [31] on investigating vulnerabilities of anchor-free detectors.

Attacking an anchor-free detector is very different from attacking an anchor-based detector. Adversarial attacks on anchor-based detectors work on selected top proposals from a set of anchors of objects, while anchor-free object detectors return only objects’ keypoints via the heatmap mechanism (see the second row in Fig. 1). These keypoints are used to generate corresponding bounding boxes. This detection procedure is completely different from anchor-based detectors, making anchor-based adversarial attacks unable to directly adapt to attack anchor-free detectors. In addition, many attack methods for anchor-based detectors such as DAG and UEA suffer from the following shortcomings. First, their generated adversarial examples have a poor transferability, *e.g.*, adversarial examples generated by DAG on Faster-RCNN can hardly be transferred to attack other object detectors. Second, some of them attack only one proposal at a time, which is extremely costly in computation. Thus, it is desired to investigate new efficient

Yunxu Xie, Quanyu Liao, and Xi Wu are with the Chengdu University of Information Technology, China. e-mail:({xieyunxu, xi.wu}@imde.ac.cn)

Shu Hu is with Carnegie Mellon University, USA. e-mail:shuhu@cmu.edu
Xin Wang and Siwei Lyu are with University at Buffalo, SUNY, USA. e-mail:({xwang264, siweilyu}@buffalo.edu)

Bin Zhu is with Microsoft Research Asia. e-mail:(binzhu@microsoft.com)

* Equal contribution. [‡] Corresponding authors.

and effective attack schemes for anchor-free detectors.

In this work, we propose a novel untargeted adversarial attack, called *Category-wise Attack*, to attack anchor-free detectors. Our proposed attack focuses on categories and can attack all objects from the same category simultaneously by attacking a set of important target pixels (see the third row in Fig. 1). The important target pixel set includes detected pixels that are highly informative (higher-level information of objects) as well as undetected pixels that have a high probability to be detected.

Our category-wise attack is formulated as a general framework that minimizes L_p norm-based perturbations, where $p \in \{0, \infty\}$, to flexibly generate sparse and dense perturbations, called *sparse category-wise attack* (SCA) and *dense category-wise attack* (DCA), respectively. Moreover, in DCA, we explore three attack strategies based on different attack regions: DCA on the global region (DCA-G) that attacks the whole region of an image, DCA on the local region (DCA-L) that attacks only important regions around objects, and DCA on the semantic region (DCA-S) that attacks semantic-rich regions of objects. Attacking only specific important regions can effectively reduce the number of pixels disturbed while retaining high attack performance.

We demonstrate the effectiveness of our methods in attacking anchor-free detector CenterNet [20] with different backbones in both object detection and human pose estimation tasks using large scale benchmark datasets: PascalVOC [32], MS-COCO [33], and COCO-keypoints [33]. Our experimental results show that our attack methods outperform existing SOTA methods with high attack performance and low visibility of perturbations.

The main contributions of our work can be summarized as follows:

- 1) We present the first algorithms of untargeted adversarial attacks on anchor-free detectors. They attack all objects in the same category simultaneously instead of only one object at a time, which avoids perturbation over-fitting on one object and increases the transferability of generated adversarial examples.
- 2) Our category-wise attack is designed to attack important pixels in images. On one hand, it can generate sparse adversarial perturbations to increase imperceptibility of generated adversarial examples. On the other hand, it can generate dense adversarial perturbations to improve attacking effectiveness.
- 3) Our method generates more transferable adversarial examples than existing attacks in both object detection and human pose estimation tasks. Our experiments on large-scale benchmark datasets indicate that it achieves the SOTA performance for both white-box and black-box attacks.

This paper extends our published conference papers [30] (ICME 2021) and [31] (IJCNN 2020) substantially in the following aspects: 1) We provide a general DCA algorithm that includes three attacking approaches based on the targeted attacking region. In particular, we propose a new DCA method called DCA-S that restricts perturbations in the semantic region, which is extracted according to informative

gradients. DCA-S can generate more semantically meaningful perturbations. 2) We show the applicability of our SCA and DCA attack methods in a practical human pose estimation task on the MS-COCO Keypoints dataset and demonstrate that they outperform existing attack methods. 3) We add more experiments to verify the effectiveness of our proposed attacking methods, especially for DCA-S. We also add more studies for analyzing the sensitivity of hyperparameters.

The rest of the paper is organized as follows. In Section II, we discuss the difference between anchor-free and anchor-based detectors and summarize existing adversarial attacks that are related to this work. In Section III, we formulate our attacking problem in the category-wise attack setting for anchor-free detectors. In Section IV, we provide a detailed description of our proposed category-wise attack in terms of sparse and dense settings. In Section V, we conduct experiments to demonstrate the efficiency and effectiveness of our proposed algorithms for attacking anchor-free detectors in both object detection and human pose estimation tasks. Section VI concludes the paper with discussions.

II. RELATED WORK

A. Anchor-based and Anchor-free Detectors

A great progress has been made in object detection in recent years. With the development of deep convolutional neural networks, many object detection approaches have been proposed. One of the most popular groups of object detection methods is the RCNN [34] family, such as Faster-RCNN [19]. The first process of RCNN's pipeline is to generate a large number of proposals based on anchors. Then a different classifier is used to classify the proposals. At last, a post-processing algorithm, such as non-maximum suppression (NMS) [35], is used to reduce redundancy proposals. Other typical anchor-based object detectors include YOLOv2 [23] and SSD [21]. They need to place a set of rectangles with pre-defined sizes during the training and then put them in some desired positions. Anchor-base detectors have high detection accuracy but also have the following shortcomings: anchor boxes should be manually defined before the training and these anchor boxes may not coincide and be consistent with ground-truth boxes.

To solve these shortcomings, anchor-free object detectors have been proposed, such as CornerNet [26] and CenterNet [20]. These object detectors detect objects by detecting their keypoints. Specifically, CornerNet detects an object by detecting the two corners of the object, and CenterNet detects objects by finding their center points. No anchor is used in both detectors. These two detectors not only are faster and simpler to train than anchor-based detectors but also achieve SOTA detection performance. Both CornerNet and CenterNet can use multiple convolutional neural networks as the backbone network to extract semantic features of an input image. Keypoints of objects are then located through these features. Normally, a keypoint includes the size and category (or class) information of its object. At last, some post-processing algorithm is used to remove redundancy keypoints. With its good keypoint estimation, CenterNet works not only for object detection but also for human pose estimation.

B. Adversarial Attacks on Object Detection

Goodfellow et al. [7] first showed the adversarial example problem of deep neural networks. An adversarial example is an original sample perturbed with deliberately crafted perturbation, typically imperceptible, that makes the DNN model predict incorrectly. Adversarial attacks can be classified into two groups: targeted adversarial attacks and untargeted adversarial attacks. A former attack aims to make the DNN model to mispredict to a specific label while a latter attack aims to make the DNN model to mispredict to anything different from the original label (including failure to detect objects for object detection). Our proposed attack is an untargeted adversarial attack.

Most adversarial attacks focus on minimizing the L_p ($p \in (0, 1, 2, \infty)$) norm of the adversarial perturbation, aiming to make the perturbation imperceptible while maintaining a high attack success rate. Typical adversarial attacks include Fast Gradient Sign Method (FGSM) [7], Project Gradient Descent (PGD) [9], and DeepFool [8]. Specifically, FGSM computes the gradient of the loss with respect to the input image to generate the adversarial perturbation as follows:

$$\bar{\mathbf{x}} = \mathbf{x} + \epsilon \cdot \text{sign}(\nabla_{\mathbf{x}} J(f(\mathbf{x}), y)),$$

where f is the classifier, J is the loss function, \mathbf{x} is the original input image, y is the ground-truth label of the input image, $\bar{\mathbf{x}}$ is the perturbed image, and ϵ is the amplitude of the perturbation. PGD applies FGSM iteratively with a smaller amplitude of the perturbation α :

$$\mathbf{x}_t = \Pi_{B_\epsilon(\mathbf{x})}(\mathbf{x}_{t-1} + \alpha \cdot \text{sign}(\nabla_{\mathbf{x}} J(f(\mathbf{x}_{t-1}), y))),$$

where $\mathbf{x}_0 = \mathbf{x}$ and $\Pi_{B_\epsilon(\mathbf{x})}(\cdot)$ is the projection function that projects the perturbed image back into the ϵ -ball centered at the original input image \mathbf{x} if necessary. DeepFool uses a generated hyperplane to approximate the decision boundary and computes the lowest Euclidean distance between the input image and the hyperplane iteratively. It then uses the distance to generate the adversarial perturbation.

The above attack methods mainly attack classifiers. Adversarial attacks on object detectors have also been proposed, such as DAG [13] and UEA [12]. They all focus on attacking anchor-base object detectors such as Faster-RCNN and SSD. The main shortcomings of these adversarial attacks are slow and not robust for transferring attacks. Furthermore, they are designed for attacking anchor-based detectors and don't work well for attacking anchor-free object detectors. To the best of our knowledge, there are no published adversarial attack on anchor-free detectors except our two conference papers [30], [31] that this paper extends.

III. PROBLEM FORMULATION

In this section, we define our optimization problem of attacking anchor-free detectors based on category-wise attacks.

Suppose there exist k object categories, $\mathcal{C} := \{C_1, C_2, \dots, C_k\}$, with detected object instances. Let $[k] := \{1, \dots, k\}$. We use S_i to denote the target pixel set of category C_i whose detected object instances will be attacked. There are k target pixel sets, $\mathcal{S} := \{S_1, S_2, \dots, S_k\}$. The

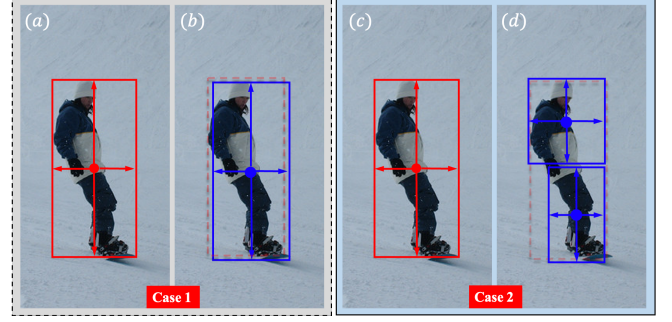


Fig. 2: Detection results before and after attacking only detected pixels. **Red** boxes denote originally detected keypoints and bounding boxes before the attack. **Blue** boxes denote newly detected keypoints after the attack. **(a) & (c)**: a detected object and a detected keypoint at the center of the person before the attack in cases 1 and 2. **(b) & (d)**: detection results after attacking only detected pixels. In case 1, after attacking all detected pixels, a neighboring pixel of the previously detected keypoint is detected as the correct category. In case 2, the centers of the top half and the bottom half of the person appear as newly detected keypoints still detected as a person. In both cases, mAP is barely reduced.

category-wise attack for anchor-free detectors is formulated as the following constrained optimization problem:

$$\begin{aligned} & \underset{\mathbf{r}}{\text{minimize}} \quad \|\mathbf{r}\|_p, \\ & \text{s.t.} \quad \arg \max_j f_j(\mathbf{x} + \mathbf{r}, s) \neq C_i, s \in S_i, \forall i \in [k], \end{aligned} \quad (1)$$

where \mathbf{r} is an adversarial perturbation, $\|\cdot\|_p$ is the L_p norm, \mathbf{x} is a clean input image, $\mathbf{x} + \mathbf{r}$ is an adversarial example, $f(\mathbf{x} + \mathbf{r}, s)$ is the classification prediction score vector for pixel s and $f_j(\mathbf{x} + \mathbf{r}, s)$ is its j -th value, where $j \in [k]$, and $\arg \max_j f_j(\mathbf{x} + \mathbf{r}, s)$ denotes the predicted object category on a target pixel $s \in S_i$ of adversarial example $\mathbf{x} + \mathbf{r}$. While p in the L_p norm can take different values, we focus on $p \in \{0, \infty\}$ in this paper.

In solving Eq. 1, it is natural to use all *detected pixels* of category C_i as target pixel set S_i . The detected pixels are selected from the heatmap of category C_i generated by an anchor-free detector such as CenterNet [20] with their probability scores higher than the detector's preset visual threshold and being detected as right objects. Unfortunately, it does not work: after attacking all detected pixels to predict into wrong categories, we expect that the detector should not detect any correct object, but our experiments with CenterNet turn out that it still can.

Further investigation enables us to explain the unexpected result as follows:

- 1) Unattacked neighboring background pixels of the heatmap can become detected pixels of the correct category. Since their detected box is close to the old detected object, CenterNet can still detect the object even though all the previously detected pixels are attacked into wrong categories. An example is shown in Fig. 2 (a) and (b).
- 2) CenterNet regards center pixels of an object as keypoints. After attacking detected pixels located around the center of an object, newly detected pixels may appear in other positions of the object, making the detector still be able to detect multiple local parts of the correct object with barely reduced mAP. An example is shown in Fig. 2 (c)

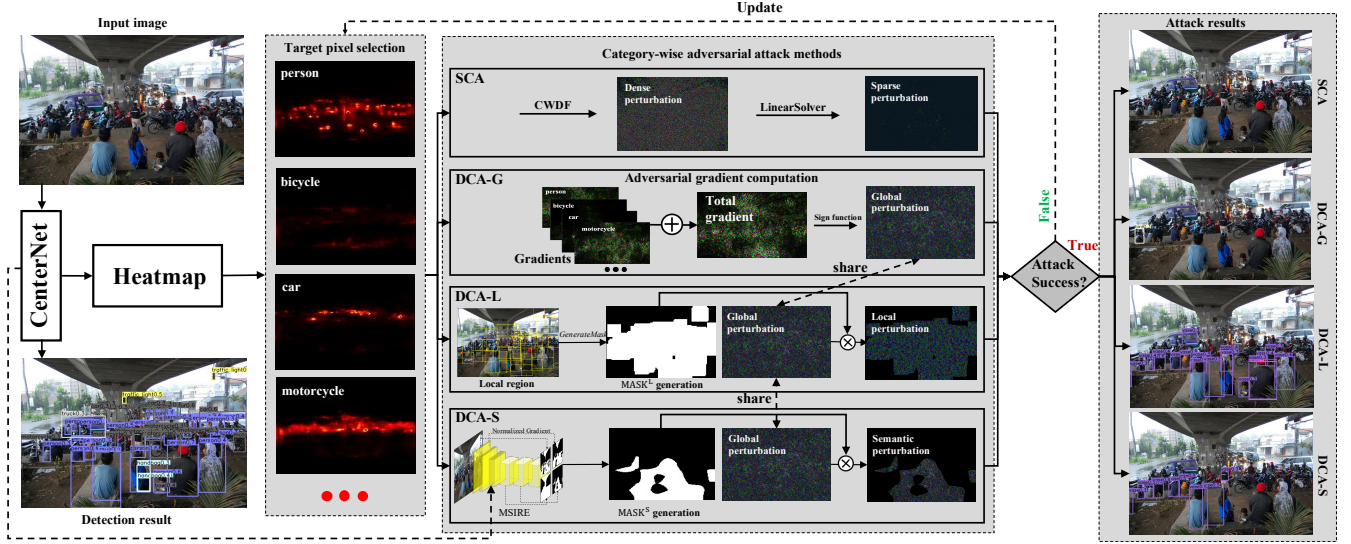


Fig. 3: Our general attack framework overview. Firstly, we extract the heatmap for each object category. Target pixels are selected based on heatmap and attacking threshold \mathcal{T} . Secondly, our proposed category-wise adversarial attack methods including sparse category-wise attack (SCA) and dense category-wise Attacks (DCA-G, DCA-L, and DCA-S) are used to attack target pixels from each category. More details about these methods can be found in the main paper. Finally, target pixel sets will be updated and the perturbation will be delicately modified if the attack is not complete. Otherwise, the attack results will output.

and (d).

Pixels that can produce one of the above two changes are referred to as *runner-up pixels*. We find that almost all *runner-up pixels* have a common characteristic: their probability scores are only a little below the visual threshold used in the object detector. Based on this characteristic, our category-wise attack methods set an attacking threshold, \mathcal{T} , lower than the visual threshold, and select all the pixels from the heatmap whose probability score is above \mathcal{T} into S_i . Therefore, S_i includes all detected and *runner-up pixels*. In this way, we can improve the transferability of generated adversarial examples.

IV. METHODOLOGY

In this section, we provide a detailed description of our category-wise attack, which is a sparse category-wise attack (SCA) if L_0 is used and a dense category-wise attack (DCA) if L_∞ is used. In DCA, we explore and design three attack strategies called DCA on the global region (DCA-G), DCA on the local region (DCA-L), and DCA on the semantic region (DCA-S). An overview of the proposed category-wise attack (CA) is shown in Fig. 3. In the following description of our methods, we focus on untargeted adversarial attack tasks. If the task is a targeted adversarial attack, our methods can be described in a similar manner.

A. Sparse Category-wise Attack (SCA)

The goal of the sparse category-wise attack is to fool the detector while perturbing a minimum number of pixels in the input image. It is equivalent to setting $p = 0$ in Eq. 1. Unfortunately, this is an NP-hard problem. To solve this problem, SparseFool [11] relaxes this NP-hard problem by iteratively approximating the classifier as a local linear function in generating sparse adversarial perturbation for image classification. Motivated by the success of SparseFool on

Algorithm 1 Category-Wise DeepFool (CWDF)

Input: image \mathbf{x} , target pixel set S_h, \mathcal{T}

Output: dense adversarial example \mathbf{x}^B

Initialize: $\mathbf{x}_1 \leftarrow \mathbf{x}, p \leftarrow 1$

while $S_h \neq \emptyset$ **do**

for $j \neq h$ **do**

$$\mathbf{v}_j \leftarrow \nabla \sum_{s \in S_h} f_j(\mathbf{x}_p, s) - \nabla \sum_{s \in S_h} f_h(\mathbf{x}_p, s)$$

$$\text{score}_j \leftarrow \sum_{s \in S_h} f_j(\mathbf{x}_p, s)$$

end for

$$o \leftarrow \underset{j \neq h}{\text{argmin}} \frac{|\text{score}_j|}{\|\mathbf{v}_j\|_2}, \mathbf{x}_{p+1} \leftarrow \mathbf{x}_p + \frac{|\text{score}_o|}{\|\mathbf{v}_o\|_2^2} \mathbf{v}_o$$

$$S_h = \text{RemovePixels}(\mathbf{x}_p, \mathbf{x}_{p+1}, S_h, \mathcal{T}) \quad /*\text{Refer to Eq. 6}*/$$

$$p \leftarrow p + 1$$

end while

return $\mathbf{x}^B \leftarrow \mathbf{x}_p$

image classification, we propose Sparse Category-wise Attack (SCA) to generate sparse perturbations for anchor-free object detectors. It is an iterative process. In each iteration, one target pixel set is selected to attack.

More specifically, given an input image \mathbf{x} and current category-wise target pixel sets \mathcal{S} , the pixel set S_h that has the highest probability score from \mathcal{S} is selected, where $h \in [k]$. We can formulate S_h as

$$S_h = \arg \max_{S_i} \left\{ \sum_{s \in S_i} f_i(\mathbf{x}, s) \mid S_i \in \mathcal{S}, i \in [k] \right\}. \quad (2)$$

Then we apply the *Category-Wise DeepFool* (CWDF) method, whose algorithm is described in Algorithm 1, to generate a dense adversarial example \mathbf{x}^B for \mathbf{x} by computing

perturbation on S_h as follows,

$$\mathbf{x}^B = \text{CWDF}(\mathbf{x}, S_h, \mathcal{T}). \quad (3)$$

CWDF is adapted from DeepFool [8] to enable it to attack all pixels from target pixel set S_h simultaneously. After the generation, we remove successfully attacked pixels from S_h .

Next, SCA uses the *ApproxBoundary* from [11] to approximate the decision boundary locally with a hyperplane β passing through \mathbf{x}^B : $\beta \triangleq \{\mathbf{x}' : \mathbf{w}^T(\mathbf{x}' - \mathbf{x}^B) = 0\}$, where \mathbf{w} is the normal vector of hyperplane β :

$$\begin{aligned} \mathbf{w} &= \text{ApproxBoundary}(\mathbf{x}^B, \mathbf{x}, S_h) \\ &= \frac{\nabla \sum_{s \in S_h} [f_{\arg \max_j f_j(\mathbf{x}^B, s)}(\mathbf{x}^B, s) - f_{\arg \max_j f_j(\mathbf{x}, s)}(\mathbf{x}^B, s)]}{\|\nabla \sum_{s \in S_h} [f_{\arg \max_j f_j(\mathbf{x}^B, s)}(\mathbf{x}^B, s) - f_{\arg \max_j f_j(\mathbf{x}, s)}(\mathbf{x}^B, s)]\|_2}. \end{aligned} \quad (4)$$

Sparse adversarial example \mathbf{x}^{adv} can then be computed via the *LinearSolver* process from [11]:

$$\mathbf{x}^{adv} = \text{LinearSolver}(\mathbf{x}, \mathbf{w}, \mathbf{x}^B). \quad (5)$$

Specifically, in each iteration, we project \mathbf{x} towards one single coordinate of \mathbf{w} . If the projection in a specific direction has no solutions, then we will ignore that direction in the next iteration because it cannot provide a significant contribution to the final perturbed image. More details can be found in [11]. For completeness, we include the algorithm of *LinearSolver* in Appendix A. The process of generating perturbation through the *ApproxBoundary* and the *LinearSolver* of SCA is illustrated in Fig. 4.

After attacking S_h through the above operations, SCA updates S_h by removing pixels that are no longer detected. This process is called *RemovePixels*. Specifically, taking \mathbf{x} , \mathbf{x}^{adv} , and S_h as input, *RemovePixels* first generates a new heatmap for perturbed image \mathbf{x}^{adv} with the detector. Then, it checks whether the probability score of each pixel in S_h is still higher than \mathcal{T} on the new heatmap. Pixels whose probability score is lower than \mathcal{T} are removed from S_h , while the remaining pixels are retained in S_h . Target pixel set S_h is thus updated. We can formulate the *RemovePixels* procedure as follows,

$$\begin{aligned} S_h &= \text{RemovePixels}(\mathbf{x}, \mathbf{x}^{adv}, S_h, \mathcal{T}) \\ &= \left\{ s \mid \arg \max_j f_j(\mathbf{x}^{adv}, s) = \arg \max_j f_j(\mathbf{x}, s), \right. \\ &\quad \left. f_{\arg \max_j f_j(\mathbf{x}^{adv}, s)}(\mathbf{x}^{adv}, s) > \mathcal{T}, s \in S_h \right\}. \end{aligned} \quad (6)$$

We iteratively execute the above procedures (i.e., Eqs. 2, 3, 4, 5, and 6) until $S \in \emptyset$, i.e., there is no correct object can be detected after the attack. The attack for all objects of \mathbf{x} is thus successful, and we output the final generated adversarial example.

The SCA algorithm is summarized in Algorithm 2. In an iteration, if SCA fails to attack any pixels of S_h in the inner loop, SCA will attack the same S_h in the next iteration. During this process, SCA keeps accumulating perturbations on these pixels, with the probability score of each pixel in S_h keeping reducing, until the probability score of every pixel in S_h is lower than \mathcal{T} . By then, S_h is attacked successfully.

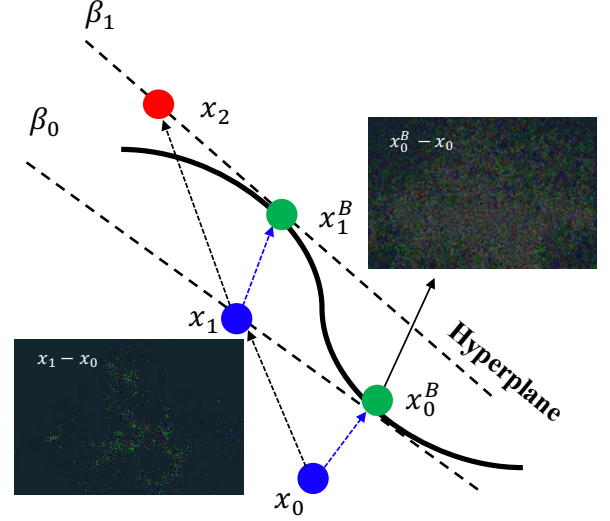


Fig. 4: Illustration of the *ApproxBoundary* and the *LinearSolver* of SCA. The black solid line denotes the real decision boundary of the object detector. Blue points denote adversarial examples that have not attacked all objects successfully. Red point denotes adversarial examples that have already attacked all objects successfully. This figure illustrates two iterations of the attack, $\mathbf{x}_0 \rightarrow \mathbf{x}_1$ and $\mathbf{x}_1 \rightarrow \mathbf{x}_2$. Take $\mathbf{x}_0 \rightarrow \mathbf{x}_1$ as an example, SCA first generates a dense adversarial example \mathbf{x}_0^B (green point) by CWDF and approximated linear decision boundary β_0 (black dash line). Then it uses *LinearSolver* to add a sparse perturbation to support \mathbf{x}_0 to approximate decision boundary β_0 by satisfying $\beta_0 = \{\mathbf{x}' : \mathbf{w}^T(\mathbf{x}' - \mathbf{x}_0^B) = 0\}$ until a valid sparse adversarial example \mathbf{x}_1 is obtained. The right image represents the perturbation after applying CWDF. The left image represents the perturbation after applying the *ApproxBoundary* and the *LinearSolver*. Comparing these two images, it is clear that the perturbation becomes sparse.

B. Dense Category-wise Attack (DCA)

It is interesting to investigate our optimization problem Eq. 1 for $p = \infty$. In this case, our adversarial perturbation generation procedure is based on PGD [36] and is called *Dense Category-wise Attack* (DCA) since it generates dense perturbations compared with SCA. Note that our DCA framework can also be based on other adversarial attacks, e.g., FGSM [37]. We propose three methods based on DCA, i.e., DCA-G, DCA-L, and DCA-S, depending on the targeted region. They are described in details next.

1) *DCA on Global Region (DCA-G)*: Given an input image \mathbf{x} and category-wise target pixel sets \mathcal{S} , DCA applies two iterative loops to generate adversarial perturbations. In each inner loop iteration j , DCA first computes the total loss of all pixels in target pixel set S_j corresponding to each available category C_j with $\sum_{s \in S_j} \text{CE}(f(\mathbf{x}, s), C_j)$, where $\text{CE}(\cdot, \cdot)$ is the traditional cross-entropy loss. Then, it computes local adversarial gradient \mathbf{g}_j of the loss with respect to the current image \mathbf{x} and normalize it with L_∞ norm:

$$\mathbf{g}_j = \frac{\nabla_{\mathbf{x}} \sum_{s \in S_j} \text{CE}(f(\mathbf{x}, s), C_j)}{\|\nabla_{\mathbf{x}} \sum_{s \in S_j} \text{CE}(f(\mathbf{x}, s), C_j)\|_\infty}.$$

After that, DCA adds up all \mathbf{g}_j to generate a total adversarial gradient G . In an outer loop iteration p , DCA computes the global perturbation (GP) by applying *sign* operation to the

Algorithm 2 Sparse Category-wise Attack (SCA)**Input:** image \mathbf{x} , \mathcal{S} , max_iter_outer , max_iter_inner **Output:** adversarial example \mathbf{x}^* , perturbation \mathbf{r} **Initialize:** $\mathbf{x}_1 \leftarrow \mathbf{x}, p \leftarrow 1$ **while** $\mathcal{S} \neq \emptyset$ and $p \leq max_iter_outer$ **do** Compute S_h with Eq. (2) and $\mathbf{x}_p, q \leftarrow 0, \mathbf{x}_{p,q} \leftarrow \mathbf{x}_p$; **while** $q \leq max_iter_inner$ and $S_h \neq \emptyset$ **do** $\mathbf{x}_{p,q}^B = \text{CWDF}(\mathbf{x}_{p,q}, S_h, \mathcal{T})$ /*See Alg. 1*/ $\mathbf{w} = \text{ApproxBoundary}(\mathbf{x}_{p,q}^B, \mathbf{x}_{p,q}, S_h)$ /*See Eq. 4*/ $\mathbf{x}_{p,q}^{adv} = \text{LinearSolver}(\mathbf{x}_{p,q}, \mathbf{w}, \mathbf{x}_{p,q}^B)$ /*See Eq. 5*/ $S_h = \text{RemovePixels}(\mathbf{x}_{p,q}, \mathbf{x}_{p,q}^{adv}, S_h, \mathcal{T})$ /*See Eq. 6*/ $q = q + 1$ **end while** $\mathbf{x}_{p+1} \leftarrow \mathbf{x}_{p,q-1}^{adv}, p = p + 1$ **end while****return** $\mathbf{x}^* = \mathbf{x}_p, \mathbf{r} = \mathbf{x}_p - \mathbf{x}$ total adversarial gradient G [36] as follows,

$$\text{GP} = \frac{\epsilon}{max_iter} \cdot \text{sign}(G), \quad (7)$$

where max_iter denotes the maximum number of iterations of the outer loop and the term $\frac{\epsilon}{max_iter}$ is perturbation size in each iteration [37]. At the end of the outer loop, DCA uses *RemovePixels* of Eq. 6 to remove from \mathcal{S} the target pixels that have already been attacked successfully on the perturbed image. Since DCA works on the global (whole) region in the original image, we call this method, DCA-G, in short. The pseudo-code of DCA-G is described in Algorithm 3.

2) *DCA on Local Region (DCA-L)*: As we discussed before, runner-up pixels are usually located near keypoints in the heatmap. They are the most important pixels for the object. In addition, perturbations in the background from an image may not impact the detection results since they are not related to the objects. To attack these objects, we only need to attack these significant pixels (i.e., runner-up and keypoints).

To fulfil the goal, we can use attack mask MASK^L to restrict perturbation around detected objects in order to disallow perturbation in the background. Attack mask MASK^L is generated from \mathcal{S} with the following process, called the *GenerateMask* procedure. MASK^L is initialized with a zero matrix of the same size as the input image. We locate each pixel point $s \in S_i, \forall i \in [k]$, on the input image and set the same location point of MASK^L to be 1. After processing all s , for each pixel $s = 1$ in MASK^L , we set all the points in the square box centered at s 's with the size of radius (side length) R^* to be 1 too. The resulting MASK^L is used as the local attack mask. The attack performance depends on the value of R^* . We will quantitatively analyze this dependence in the experimental studies reported in Section V-C.

A local perturbation (LP) is obtained by applying MASK^L

Algorithm 3 Dense Category-wise Attack (DCA)**Input:** image \mathbf{x} , \mathcal{S} , \mathcal{C} , ϵ , max_iter , \mathcal{T} **Output:** adversarial example \mathbf{x}^* , perturbation \mathbf{r} **Initialize:** $\mathbf{x}_1 \leftarrow \mathbf{x}, p \leftarrow 1$ **while** $\mathcal{S} \neq \emptyset$ and $p \leq max_iter$ **do** $G \leftarrow 0, j \leftarrow 1$ **while** $j \leq k$ **do** **if** $S_j \neq \emptyset$ **then**

$$\mathbf{g}_j = \frac{\nabla_{\mathbf{x}_p} \sum_{s \in S_j} \text{CE}(f(\mathbf{x}_p, s), C_j)}{\|\nabla_{\mathbf{x}_p} \sum_{s \in S_j} \text{CE}(f(\mathbf{x}_p, s), C_j)\|_\infty}, G \leftarrow G + \mathbf{g}_j$$
 end if $j \leftarrow j + 1$ **end while** $\text{GP} \leftarrow \frac{\epsilon}{max_iter} \cdot \text{sign}(G)$ **if** DCA-G **then** $\mathbf{x}_{p+1} \leftarrow \mathbf{x}_p + \text{GP}$ /*Refer to Eq. 7*/ **else if** DCA-L **then** $\mathbf{x}_{p+1} \leftarrow \mathbf{x}_p + \text{GP} * \text{MASK}^L$ /*Refer to Eq. 8*/ **else if** DCA-S **then** $\mathbf{x}_{p+1} \leftarrow \mathbf{x}_p + \text{GP} * \text{MASK}^S$ /*Refer to Eq. 9*/ **end if** **for** S_i in \mathcal{S} **do** $S_i = \text{RemovePixels}(\mathbf{x}_p, \mathbf{x}_{p+1}, S_i, \mathcal{T})$ /*Refer to Eq. 6*/ **end for** $p \leftarrow p + 1$ **end while****return** $\mathbf{x}^* = \mathbf{x}_p, \mathbf{r} = \mathbf{x}_p - \mathbf{x}$

on the global perturbation (GP):

$$\text{LP} = \text{GP} * \text{MASK}^L. \quad (8)$$

After generating LP, we update \mathcal{S} by removing the points that have been attacked successfully with *RemovePixels* (Eq. 6). The pseudo-code of DCA-L is shown in Algorithm 3.

3) *DCA on Semantic Region (DCA-S)*: Using DCA on the local region may not get a perfect perturbation around objects because run-up pixels may not be all around objects since some of them may not represent semantic information of objects. In addition, DCA-L uses a regular square mask around each pixel in $\mathcal{S}, \forall i \in [k]$, which may not precisely select important perturbation signals from the global perturbation, as Fig. 5 shows. To address this issue, we propose the DCA-S method that applies DCA to the semantic region of the image.

Since convolutional layers of the CNN-based anchor-free model contain abundant information, especially the spatial information [38], [39], which can indicate which regions of an input image have a higher response to the output of the classifier. This characteristic demonstrates that the generated perturbation will be more effective if we only attack pixels that are related to the semantic region of objects. A natural strategy

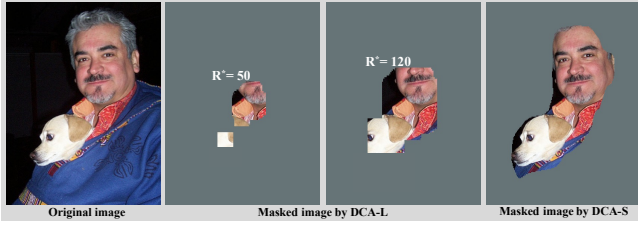


Fig. 5: Comparison of masks from DCA-L and DCA-S. A proper radius R^* of the DCA-L mask is hard to be determined. A undersized R^* (i.e., $R^*=50$) will miss some important regions (e.g., human and dog faces) while an oversized R^* (i.e., $R^*=120$) will introduce more useless local perturbations (e.g., perturbations on background), which may lead to worse results. In contrast, the mask generated by DCA-S is more precise.

for getting this semantic region is to extract the feature map based on the convolutional layer outputs [40]–[42]. Shallower layers usually keep much spatial information, leading to a sparse and discontinuous high response region in the feature map. On the other hand, deeper layers contain more global information due to their larger receptive fields, resulting in a large and continuous high response region.

In prior work [39], the last convolutional layer is used to adopt the key region. Discarding spatial information from shallower layers makes this method hard to accurately target locations of small objects. Inspired by [40]–[42], we propose a multi-layer semantic information region selection (MSIRE) method, to be described in detail next, to extract and integrate semantic information from both deep and shallow layers. By integrating the gradient information from these layers, we can construct a semantic mask that contains the most informative semantic region of objects, which is then combined with the global perturbation (GP) to generate the final perturbation.

Now we describe the MSIRE method. Let $L = \{l_i\}_{i=1}^n$ be the set of layers that we consider to extract key region, where l_i is the i -th layer containing feature map activations h_i . In our experiments, n is set to 4. For layer l_i , we calculate and sum the gradient of the score for category C_j of all pixels in target pixel set S_j with respect to its feature map activation h_i , and sum them up across all categories,

$$G_i = \sum_{j \in [k]} \frac{\partial \sum_{s \in S_j} f_j(\mathbf{x}, s)}{\partial h_i}$$

Then normalize gradient G_i to $[0,1]$ and upsample to the size of image \mathbf{x} :

$$\hat{G}_i = \Phi\left(\frac{G_i - \min(G_i)}{\max(G_i) - \min(G_i)}\right),$$

where $\Phi(\cdot)$ denotes the operation of upsampling and $\min(G_i)$ and $\max(G_i)$ are the minimal and maximal value of elements in G_i , respectively. The mask corresponding to layer l_i can be obtained using a threshold \mathcal{T}_s :

$$mask_i = \delta(\hat{G}_i > \mathcal{T}_s),$$

where $\delta(\cdot)$ is an impulse response that turns a pixel greater than \mathcal{T}_s to 1, otherwise to 0. Combining $mask_i, \forall i \in [n]$ as

$$MASK^S = \prod_{i=1}^n mask_i,$$

where $MASK^S$ denotes the final semantic region attack mask.

After obtaining $MASK^S$, we combine it with the global perturbation (GP) to get a semantic region guided perturbation (SP) as follows,

$$SP = GP * MASK^S. \quad (9)$$

Like its siblings, after generating the perturbation, DCA-S updates \mathcal{S} with *RemovePixels* (Eq. 6). The pseudo-code of DCA-S is shown in Algorithm 3.

V. EXPERIMENTS

In this section, we will evaluate the performance of the proposed adversarial attack (i.e., SCA, DCA-G, DCA-L, and DCA-S) for both object detection and human pose estimation based on anchor-free detector CenterNet [20].

A. Experimental Settings

1) *Detectors and Datasets*: For object detection, we evaluate our proposed attack on two public datasets: PascalVOC [32] and MS-COCO [33]. We use the two pre-trained detectors (CenterNet with two different backbones: ResNet18 (R18) [43] and DLA34 [44]) from [20] in our experiments. These two detectors are pre-trained on the training set of PascalVOC (including PascalVOC 2007 and PascalVOC 2012) and MS-COCO 2017, respectively. Our adversarial examples are generated on the test set of PascalVOC 2007, which consists of 4,592 images and 20 categories, and the validation set of MS-COCO 2017, which contains 5,000 images and 80 object categories. For human pose estimation, we use the pre-trained detector (CenterNet with DLA34 [44] backbone) from [20] that is trained on the training set of MS-COCO Keypoints 2017. Our adversarial examples are generated on its validation set, which contains 5,000 images and 17 categories of keypoints for humans.

2) *Evaluation Metrics*: We evaluate the performance of both white-box and black-box attacks with the following metrics.

- The attack performance is evaluated by computing the decreased percentage of mean average precision (mAP), referred to as the **mAP Score Degradation Ratio (ASR)**, which is defined as,

$$ASR = 1 - \frac{mAP_{attack}}{mAP_{clean}},$$

where mAP_{attack} denotes the mAP of the targeted object detector on adversarial examples, and mAP_{clean} denotes the mAP on clean samples. Higher ASR means better white-box attack performance.

- We also use the L_0 and L_2 norms of perturbation \mathbf{r} , P_{L_0} and P_{L_2} , respectively, to quantify the **perceptibility** of the adversarial perturbation. $P_{L_0} = \|\mathbf{r}\|_0$ quantifies the proportion of perturbed pixels. A lower value means that fewer image pixels are perturbed. For $P_{L_2} = \|\mathbf{r}\|_2$, a greater value usually signifies a more perceptible perturbation to humans.
- For black-box attacks, transferability of adversarial examples generated with other detectors and tested with the

target detector is used to measure the attack performance. More specifically, the attack performance of block-box attacks is measured by the ratio, referred to as the **Attack Transfer Ratio (ATR)**, of the ASR on the target model, ASR_{target} , to the ASR on the generating model, ASR_{origin} :

$$ATR = \frac{ASR_{target}}{ASR_{origin}},$$

Higher ATR means better transferability.

In our experiments, for object detection, black-box adversarial examples are generated on CenterNet with one backbone (R18 or DLA34) and tested on CenterNet with a different backbone (DLA34, R18, and ResNet101 (R101)). We also test these adversarial examples on other detectors, including anchor-free (CornerNet [26] with backbone Hourglass [45]) and anchor-based detectors (Faster-RCNN [19] and SSD [21]). For human pose estimation, all adversarial examples are generated on CenterNet with backbone DLA34 and tested on CenterNet with backbone Hourglass.

Additionally, we follow [46] to simulate a real-world attack transferring scenario, wherein generated adversarial examples are saved in the JPEG format and then reloaded to attack the target model. In real-world applications, images are usually saved in a compression format. JPEG is a most commonly used lossy compression standard for images. The transferability test in this way requires adversarial examples to be robust to the JPEG compression like in most real-world applications.

3) *Comparison Methods and Implementation Details:* For object detection, since there is no existing attack dedicated to anchor-free detectors, we use an existing state-of-the-art attack designed for attacking anchor-based detectors, i.e., DAG [13] with VGG16 [47] backbone for attacking Faster-RCNN (FR) as the attack to compare with. For human pose estimation, we compare with existing methods proposed in [48] for attacking human pose estimation systems, called FHPE and PHPE, which are based on FGSM and PGD, respectively.

Our methods are implemented with Python 3.6 and Pytorch 1.1.0. All the experiments are conducted with an Intel Core i9-7960 and an Nvidia GeForce GTX-1070Ti GPU. We set max_iter_outer , max_iter_inner , and max_iter to 50, 20, and 30, respectively. The default values of R^* , T_s , T , and ϵ are 60, 0.5, 0.1, and 5% of the maximum value of the pixels in an image, respectively. All input images are resized to 512×512 .

B. Experimental Results on Object Detection

1) *White-Box Attack Performance:* Table I shows the white-box attack results on both PascalVOC and MS-COCO.

- For *PascalVOC*, we can see that DCA-G with the DLA34 backbone achieves the best ASR. SCA with both backbones produces much smaller perturbations than other methods and DCA-G with the R18 is 14 times faster than DAG. Furthermore, while the ASR performance of both DCA-L and DCA-S are very close to that of DAG, DCA-L and DCA-S produce smaller perturbations

Data	Method	Network	mAP _{clean}	mAP _{attack}	ASR	$P_{L_2} (\times 10^{-3})$	P_{L_0}	Time (s)
PascalVOC	DAG	FR	0.70	0.050	0.92	3.20	0.990	9.8
	SCA	R18	0.71	0.060	0.91	0.41	0.002	32.5
	SCA	DLA34	0.79	0.110	0.86	0.44	0.003	117.3
	DCA-G	R18	0.71	0.070	0.90	5.20	0.990	0.7
	DCA-G	DLA34	0.79	0.050	0.94	5.10	0.990	1.2
	DCA-L	R18	0.71	0.080	0.89	2.70	0.320	1.6
	DCA-L	DLA34	0.79	0.080	0.90	2.80	0.320	3.1
	DCA-S	R18	0.71	0.070	0.90	2.40	0.260	2.2
	DCA-S	DLA34	0.79	0.060	0.92	2.20	0.280	4.0
MS-COCO	DAG	FR	0.35	0.040	0.89	5.00	0.990	20.4
	SCA	R18	0.28	0.027	0.91	0.48	0.004	50.4
	SCA	DLA34	0.37	0.030	0.92	0.49	0.007	216.0
	DCA-G	R18	0.28	0.002	0.99	5.80	0.990	2.4
	DCA-G	DLA34	0.37	0.002	0.99	5.90	0.990	4.9
	DCA-L	R18	0.28	0.006	0.98	3.20	0.380	3.4
	DCA-L	DLA34	0.37	0.008	0.98	3.30	0.390	6.3
	DCA-S	R18	0.28	0.003	0.99	2.80	0.300	4.7
	DCA-S	DLA34	0.37	0.004	0.99	3.00	0.310	8.5

TABLE I: White-box performance comparison. “Time” is the average time to generate an adversarial example. The best results are shown in bold.

and have lower time complexity than DAG in generating adversarial examples.

- For *MS-COCO*, both DCA-G and DCA-S achieve the highest ASR, 99.0%, which is significantly higher than that of DAG. Like on PascalVOC, the ASR performance of SCA with both R18 and DLA34 is in the same ballpark as that of DAG, SCA produces much smaller perturbations than other methods in terms of both P_{L_2} and P_{L_0} , and DCA-G is the fastest in generating an adversarial example.

In general, both SCA and DCA achieve state-of-the-art attack performance. Specifically, DCA can achieve high ASR and low time complexity, while SCA can produce much smaller perturbations without degrading ASR much. We can see that P_{L_0} of SCA is lower than 1%, implying that SCA can successfully attack detectors by perturbing only a small percentage of pixels of the original image. Comparing DCA-L and DCA-G, while it may slightly decrease the performance of ASR, DCA-L using a local region significantly decreases the size of perturbation. Comparing DCA-S and DCA-L, DCA-S not only improves the performance of ASR but also reduces the perturbation size in terms of both P_{L_2} and P_{L_0} . This implies that the DCA on the semantic region is better than it on the local region. A qualitative comparison between DAG and our methods is shown in Fig. 6. It is clear that perturbations generated by SCA and DCA-based methods are hard to be perceived by humans.

We also show in Fig. 7 the Average Precision (AP) of each object category on clean inputs and adversarial examples generated by our methods on PascalVOC with CenterNet using both R18 and DLA34 backbones. The AP drops by a roughly similar percentage for all the object categories. Fig. 8 shows the AP and Average Recall (AR) of SCA and DCA-based methods on MS-COCO with CenterNet. We can notice that small objects are more vulnerable to adversarial examples than bigger ones. One possible explanation is that bigger objects usually have more keypoints than smaller objects on the heatmap and our algorithms need to attack all of them.

2) *Black-Box Attack Performance:* In evaluating black-box attack performance, adversarial examples are generated with CenterNet using the R18 or DLA34 backbone for our proposed methods or with Faster-RCNN for DAG and tested with other

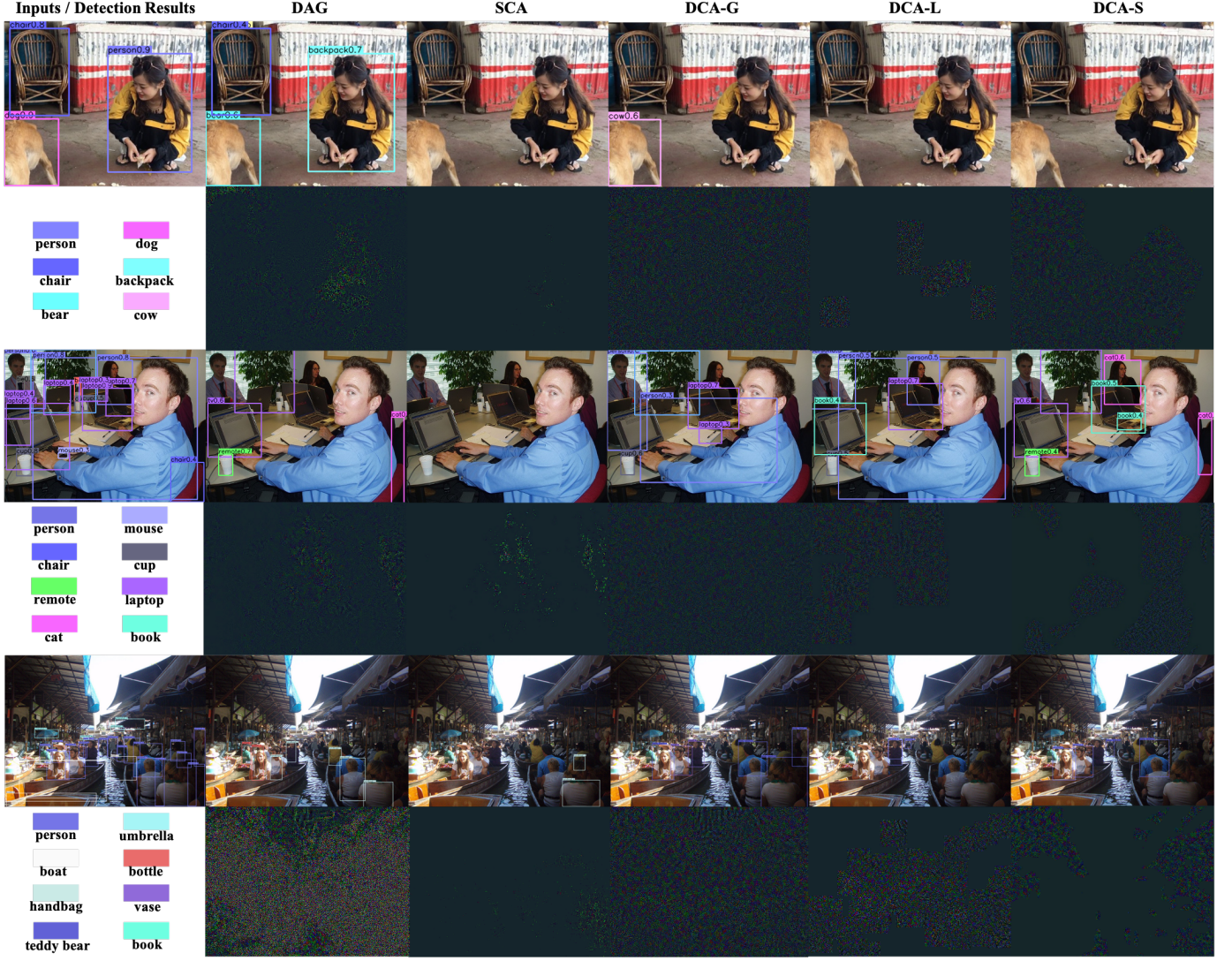


Fig. 6: Qualitative comparison between DAG and our methods on the object detection task. Three examples are presented. **Column 1:** Detection results of clean inputs. **Column 2:** DAG’s attack results and perturbations. **Column 3:** SCA’s attack results and perturbations. **Columns 4 - 6:** the attack results and perturbations of DCA-G, DCA-L, and DCA-S, respectively. The perturbations are magnified by a factor of 30 for better visibility.

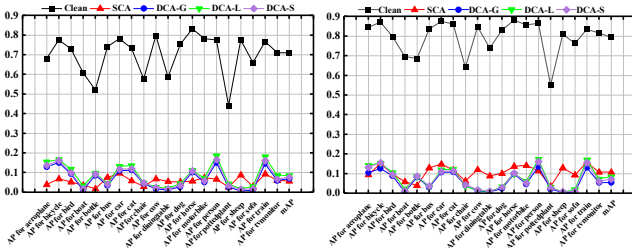


Fig. 7: The AP of each object category on clean inputs and adversarial examples generated by SCA and DCA-methods on PascalVOC with CenterNet using R18 (**left**) and DLA34 (**right**) backbones on PascalVOC.

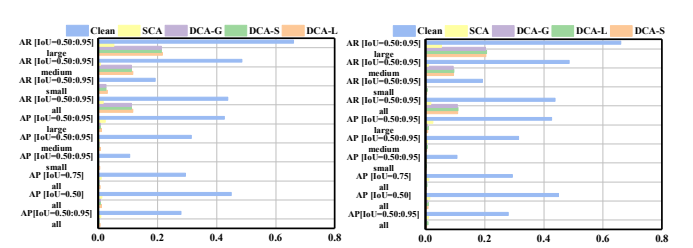


Fig. 8: The AR (**top four**) and AP (**bottom six**) performance of different sizes of objects on clean inputs and adversarial examples generated by SCA and DCA-based methods on MS-COCO with CenterNet using R18 (**left**) and DLA34 (**right**) backbones.

object detection models. Table II and Table III show the black-box attack performance on PascalVOC and MS-COCO, respectively.

- *Attack transferability on PascalVOC.* From Table II, we can see that adversarial examples generated by our methods can successfully transfer to not only CenterNet with

different backbones but also completely different types of object detectors such as Faster-RCNN and SSD. Specifically, we can see that SCA with the DLA34 backbone achieves the best ATR and SCA with the R18 backbone achieves similar ATR to the DCA-based methods with both the R18 and DLA34 backbones. on the other hand,

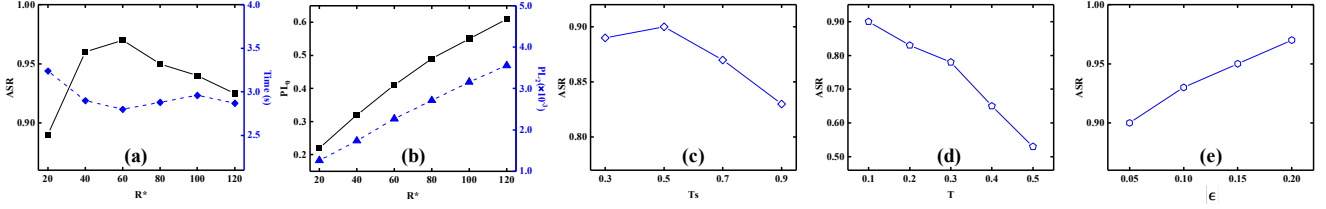


Fig. 9: Sensitivity analysis of hyperparameters.

From \ To	R18		DLA34		R101		Faster-RCNN		SSD	
	mAP	ATR	mAP	ATR	mAP	ATR	mAP	ATR	mAP	ATR
Clean	0.71	—	0.77	—	0.79	—	0.71	—	0.74	—
DAG	0.65	0.09	0.75	0.03	0.72	0.10	0.05	—	0.72	0.03
R18-SCA	0.06	—	0.62	0.21	0.61	0.25	0.55	0.25	0.70	0.10
DLA34-SCA	0.42	0.47	0.11	—	0.53	0.38	0.44	0.44	0.62	0.19
R18-DCA-G	0.07	—	0.62	0.22	0.65	0.20	0.61	0.16	0.72	0.03
DLA34-DCA-G	0.50	0.31	0.05	—	0.62	0.23	0.53	0.27	0.67	0.10
R18-DCA-L	0.08	—	0.61	0.23	0.63	0.23	0.55	0.25	0.68	0.09
DLA34-DCA-L	0.48	0.35	0.06	—	0.60	0.24	0.51	0.37	0.66	0.12
R18-DCA-S	0.07	—	0.65	0.17	0.65	0.17	0.61	0.16	0.73	0.01
DLA34-DCA-S	0.52	0.29	0.06	—	0.62	0.22	0.57	0.21	0.70	0.06

TABLE II: Black-box attack results on the PascalVOC dataset. **From**: the leftmost column denotes the models which adversarial examples are generated from. **To**: the top row denotes the target models that adversarial examples transfer to (i.e., are tested on). “—” means the value is unavailable (not defined).

From \ To	R18		DLA34		R101		CornerNet	
	mAP	ATR	mAP	ATR	mAP	ATR	mAP	ATR
Clean	0.29	—	0.37	—	0.37	—	0.43	—
DAG	0.24	0.19	0.33	0.12	0.31	0.18	0.40	0.08
R18-SCA	0.02	—	0.27	0.30	0.24	0.39	0.35	0.20
DLA34-SCA	0.07	0.82	0.03	—	0.09	0.82	0.12	0.78
R18-DCA-G	0.00	—	0.29	0.21	0.28	0.25	0.38	0.12
DLA34-DCA-G	0.10	0.67	0.00	—	0.12	0.69	0.13	0.72
R18-DCA-L	0.01	—	0.27	0.28	0.27	0.28	0.36	0.17
DLA34-DCA-L	0.10	0.67	0.01	—	0.12	0.69	0.13	0.71
R18-DCA-S	0.00	—	0.31	0.16	0.29	0.22	0.39	0.09
DLA34-DCA-S	0.12	0.59	0.00	—	0.13	0.64	0.13	0.72

TABLE III: Black-box attack results on the MS-COCO dataset. **From**: the leftmost column denotes the models which adversarial examples are generated from. **To**: the top row denotes the target models that adversarial examples transfer to (i.e., are tested on). “—” means the value is unavailable (not defined).

adversarial examples generated by DAG with Faster-RCNN have a much poorer transferability in attacking CenterNet and SSD than our proposed methods, esp. SCA with the DLA34 backbone. In addition, we can also see that our proposed methods have better transferability in attacking CenterNet and Faster-RCNN than in attacking SSD, which implies that SSD is less reliable on highly informational points in the CenterNet-generated heatmap than Faster-RCNN and CenterNet with a different backbone.

- **Attack Transferability on MS-COCO.** From Table III, we can see that adversarial examples generated with our proposed methods with the DLA34 backbone have significantly higher ATR than other methods including our proposed methods with the R18 backbone. Our proposed methods with the DLA34 backbone can attack not only CenterNet with different backbones but also CornerNet. Like on PascalVOC, DAG has a poor transferability in attacking CenterNet and CornerNet on MS-COCO too.

C. Sensitivity Analysis of Hyperparameters

In our algorithms, we have four hyperparameters that need to be tuned. To study their sensitivity, we generate adversarial examples by attacking CenterNet with the R18 backbone on MS-COCO for evaluating R^* and on PascalVOC for evaluating T_s , T , and ϵ . Then we report the performance with respect to each hyperparameter. More details are provided as follows.

1) **Sensitivity Analysis of R^* :** In DCA-L, we need to use R^* to control the size of extracted local regions. It is clear that R^* correlates with the attack performance ASR, P_{L_0} , P_{L_2} , and time consumption. We show these relationships in Fig. 9 (a) and (b). From these figures, we can draw three conclusions. First, the ASR of DCA-L correlates positively with R^* when R^* is less than 60. However, ASR is stable or slightly decreased afterward. The reason is that the oversized mask may introduce more useless perturbation, resulting in a worse effect. Second, P_{L_0} and P_{L_2} of the perturbation correlates positively with R^* . This is because higher R^* means bigger attack masks. Finally, the average attack time of DCA-L correlates negatively with R^* when R^* is lower than 48 and becomes stable afterward.

2) **Sensitivity Analysis of T_s :** In DCA-S, hyperparameter T_s is used to select semantic regions or pixels that contain more informative gradients. Fig. 9 (c) shows attack performance ASR with different T_s . We can see that the best ASR occurs when T_s is 0.5. ASR decreases when T_s increases from 0.5, which can be explained by the fact that a too large value of T_s makes the mask too small, resulting in many useful pixels related to objects excluded from the mask and thus degraded attack performance.

3) **Sensitivity Analysis of T :** The default value of the visual threshold is 0.3 in the CenterNet. We use DCA-G to evaluate the sensitivity of T . The results are reported in Fig. 9 (d). We can see that ASR shows an obvious decreasing trend when T increases. In particular, the decreasing trend becomes sharper when T is greater than 0.3, which can be explained that more runner-up points (pixels) are included in the target pixel sets if T is below 0.3, resulting in improved attacking performance. We can also see that the performance gap is more than 0.1 when T changes from 0.3 to 0.1. This implies that runner-up points have a significant impact on the attack performance. On the other hand, if T is higher than 0.3, some keypoints are excluded from the target pixel sets and thus unattacked, leading to faster degraded ASR.

4) **Sensitivity Analysis of ϵ :** We analyze the sensitivity of the amplitude of the perturbation ϵ with DCA-G. The results are reported in Fig. 9 (e). A large ϵ means a larger perturbation

Data	Method	Network	mAP _{clean}	mAP _{attack}	ASR	$P_{L_2} (\times 10^{-3})$	P_{L_0}	Time (s)
MS-COCO Keypoints	FHPE	DLA34	0.53	0.31	0.42	0.33	0.990	0.6
	PHPE	DLA34	0.53	0.11	0.79	0.20	0.990	4.2
	SCA	DLA34	0.53	0.03	0.93	0.17	0.002	130.1
	DCA-G	DLA34	0.53	0.00	1.00	0.62	0.990	11.2
	DCA-L	DLA34	0.53	0.04	0.92	0.45	0.250	12.7
	DCA-S	DLA34	0.53	0.03	0.94	0.36	0.180	15.2

TABLE IV: White-box attack results on the MS-COCO Keypoints dataset. “Time” is the average time to generate an adversarial example.

To	From	DLA34						
		Clean	FHPE	PHPE	SCA	DCA-G	DCA-L	DCA-S
Hourglass	mAP	0.58	0.50	0.36	0.18	0.26	0.23	0.24
	ATR	–	0.33	0.48	0.74	0.55	0.66	0.63

TABLE V: Black-box attack results on the MS-COCO Keypoints dataset. **To**: the leftmost column denotes the target models that adversarial examples transfer to (i.e., are tested on). **From**: the top row denotes the models which adversarial examples are generated from.

size. We expect ASR increases with increasing ϵ . This is confirmed by the experimental results shown in the figure.

D. Experimental Results on Human Pose Estimation

In the MS-COCO Keypoints dataset, there are 17 categories of keypoints for humans. We attack target pixels from each category and report the attacking performance next.

1) *White-Box Attack*: The white-box attack results on the MS-COCO Keypoints dataset are summarized in Table IV. We can see that our DCA-G has the highest ASR, which is 1. This means DCA-G has attacked all the testing images successfully. Since FHPE and PHPE are based on the conventional FGSM and PGD methods and thus very simple in terms of complexity, we expect them to have less attack time, which is confirmed by the results shown in Table IV. However, these two comparison methods have much lower ASR than our proposed methods. All of our proposed methods outperform these two baselines on the ASR metric.

On the other hand, it is clear that our SCA has the lowest P_{L_0} and P_{L_2} values, which is consistent with the observation on the object detection task. In addition, our DCA-L and DCA-S also have lower P_{L_0} and P_{L_2} values than DCA-G, which is due to the role of masks used in both DCA-L and DCA-S. A qualitative comparison between the comparison methods and our proposed methods is shown in Fig. 10.

2) *Black-Box Attack and Transferability*: The black-box attack results are reported in Table V. We can see that our SCA achieves the best transferability, which is the same as on the object detection task. Furthermore, all of our proposed methods outperform the baseline methods, which implies that our category-wise attack can improve the transferability of adversarial examples.

VI. CONCLUSION

In this work, we propose the first adversarial attack on anchor-free detectors. It is a category-wise attack that attacks important pixels of all instances of a category simultaneously. Our attack manifests in two forms, sparse category-wise attack

(SCA) and dense category-wise attack (DCA), when minimizing the L_0 and L_∞ norm-based perturbations, respectively. For SCA, it can generate sparse-imperceptible adversarial samples. For DCA, we further provide three variants, DCA-G, DCA-L, and DCA-S, to enable a flexible selection of a specific attacking region: the global region, the local region, and the semantic region, respectively, to improve the attack effectiveness and efficiency. Our experiments on large-scale benchmark datasets including PascalVOC, MS-COCO, and MS-COCO Keypoints indicate that the proposed methods achieve state-of-the-art attack performance and transferability on both object detection and human pose estimation tasks.

Limitations. There are two limitations in our proposed methods. The first limitation is that SCA has significantly higher time complexity since its Algorithm 2 includes CWDF and Linear Solver procedures. Our experimental results confirm it: SCA needs a much longer time to attack an image for both object detection and human pose estimation. The second limitation is that the transferability of our proposed methods on attacking SSD is much lower than that of our methods on attacking other models.

Future Work. First, we will try to address the aforementioned limitations of our proposed methods. Second, we plan to incorporate a scheme to automatically determine the hyperparameters. Third, we will try to develop effective defenses against the proposed attacks, which is important for practical applications of anchor-free detectors.

APPENDIX A ALGORITHM OF LINEARSOLVER

The LinearSolver algorithm is shown in Algorithm 4. In each iteration, we project towards only one single coordinate of \mathbf{w} . If projecting \mathbf{x} to a specific direction does not provide a solution, it will be ignored in the next iteration. More details can be found in [11]. Note that the projection operator of Q in Algorithm 4 controls the pixel values between 0 and 255.

Algorithm 4 LinearSolver

Input: image \mathbf{x} , normal vector \mathbf{w} , boundary point \mathbf{x}^B , projection operator Q

Output: perturbed point \mathbf{x}^{adv}

Initialize: $\mathbf{x}^0 \leftarrow \mathbf{x}$, $i \leftarrow 0$, $\mathcal{H} = \{\}$

while $\mathbf{w}^T(\mathbf{x}^i - \mathbf{x}^B) \neq 0$ **do**

$\mathbf{r} \leftarrow \mathbf{0}$

$d \leftarrow \arg \max_{j \in \mathcal{H}} |w_j|$

$r_d \leftarrow \frac{|\mathbf{w}^T(\mathbf{x}^i - \mathbf{x}^B)|}{|w_d|} \cdot \text{sign}(w_d)$

$\mathbf{x}^{(i+1)} \leftarrow Q(\mathbf{x}^i + \mathbf{r})$

$\mathcal{H} \leftarrow \mathcal{H} \cup \{d\}$

$i \leftarrow i + 1$

end while

return $\mathbf{x}^{adv} \leftarrow \mathbf{x}^i$

REFERENCES

- [1] Y. Xiang *et al.*, “Rmbench: Benchmarking deep reinforcement learning for robotic manipulator control,” *arXiv preprint arXiv:2210.11262*, 2022.



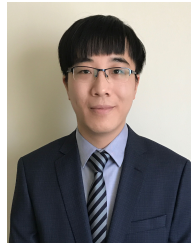
Fig. 10: Qualitative comparison between the comparison methods and our proposed methods on the human pose estimation task. Three examples are presented. **Column 1:** Detection results of clean inputs. **Column 2:** FHPE attacked results and perturbations. **Column 3:** PHPE attacked results and perturbations. **Column 4:** SCA attacked results and perturbations. **Column 5 - 7:** DCA-G, DCA-L, and DCA-S attacked results and their perturbations, respectively. The perturbations are magnified by a factor of 30 for better visibility.

- [2] W. Pu *et al.*, “Learning a deep dual-level network for robust deepfake detection,” *Pattern Recognition*, 2022.
- [3] S. Hu *et al.*, “Pseudoprop: Robust pseudo-label generation for semi-supervised object detection in autonomous driving systems,” in *CVPR Workshops*, 2022, pp. 4390–4398.
- [4] H. Guo *et al.*, “Robust attentive deep neural network for detecting gan-generated faces,” *IEEE Access*, 2022.
- [5] Z. Luo *et al.*, “Stochastic planner-actor-critic for unsupervised deformable image registration,” in *AAAI*, 2022.
- [6] S. Hu, L. Ke, X. Wang, and S. Lyu, “Tkml-ap: Adversarial attacks to top-k multi-label learning,” in *Proceedings of the IEEE/CVF International Conference on Computer Vision*, 2021, pp. 7649–7657.
- [7] I. J. Goodfellow, J. Shlens, and C. Szegedy, “Explaining and harnessing adversarial examples,” *arXiv preprint arXiv:1412.6572*, 2014.
- [8] S.-M. Moosavi-Dezfooli, A. Fawzi, and P. Frossard, “Deepfool: a simple and accurate method to fool deep neural networks,” in *CVPR*, 2016.
- [9] A. Kurakin, I. J. Goodfellow, and S. Bengio, “Adversarial examples in the physical world,” in *Artificial intelligence safety and security*. Chapman and Hall/CRC, 2018, pp. 99–112.
- [10] Y. Dong, F. Liao, T. Pang, H. Su, J. Zhu, X. Hu, and J. Li, “Boosting adversarial attacks with momentum,” in *CVPR*, 2018.
- [11] A. Modas, S.-M. Moosavi-Dezfooli, and P. Frossard, “Sparsefool: a few pixels make a big difference,” in *CVPR*, 2019.
- [12] X. Wei, S. Liang, N. Chen, and X. Cao, “Transferable adversarial attacks for image and video object detection,” *IJCAI*, 2018.
- [13] C. Xie, J. Wang, Z. Zhang, Y. Zhou, L. Xie, and A. Yuille, “Adversarial examples for semantic segmentation and object detection,” in *ICCV*, 2017.
- [14] R. Sanchez-Matilla, C. Y. Li, A. S. Shamsabadi, R. Mazzon, and A. Cavallaro, “Exploiting vulnerabilities of deep neural networks for privacy protection,” *IEEE Transactions on Multimedia*, vol. 22, no. 7, pp. 1862–1873, 2020.
- [15] T. Shermin, G. Lu, S. W. Teng, M. Murshed, and F. Sohel, “Adversarial network with multiple classifiers for open set domain adaptation,” *IEEE Transactions on Multimedia*, vol. 23, pp. 2732–2744, 2020.
- [16] S. Hu, X. Wang, and S. Lyu, “Rank-based decomposable losses in machine learning: A survey,” *arXiv preprint arXiv:2207.08768*, 2022.
- [17] C. Szegedy, W. Zaremba, I. Sutskever, J. Bruna, D. Erhan, I. Goodfellow, and R. Fergus, “Intriguing properties of neural networks,” *arXiv preprint arXiv:1312.6199*, 2013.
- [18] Y. Qian, J. Wang, B. Wang, S. Zeng, Z. Gu, S. Ji, and W. Swaileh, “Visually imperceptible adversarial patch attacks on digital images,” *arXiv preprint arXiv:2012.00909*, 2020.
- [19] S. Ren, K. He, R. Girshick, and J. Sun, “Faster r-cnn: Towards real-time object detection with region proposal networks,” in *NIPS*, 2015.
- [20] X. Zhou, D. Wang, and P. Krähenbühl, “Objects as points,” *arXiv preprint arXiv:1904.07850*, 2019.
- [21] W. Liu, D. Anguelov, D. Erhan, C. Szegedy, S. Reed, C.-Y. Fu, and A. C. Berg, “Ssd: Single shot multibox detector,” in *ECCV*. Springer, 2016.
- [22] T.-Y. Lin, P. Goyal, R. Girshick, K. He, and P. Dollár, “Focal loss for dense object detection,” in *Proceedings of the IEEE international conference on computer vision*, 2017, pp. 2980–2988.
- [23] J. Redmon and A. Farhadi, “Yolo9000: better, faster, stronger,” in *Proceedings of the IEEE conference on computer vision and pattern recognition*, 2017, pp. 7263–7271.
- [24] K. He, G. Gkioxari, P. Dollár, and R. Girshick, “Mask r-cnn,” in *CVPR*, 2017.

- [25] T.-I. Chen, Y.-C. Liu, H.-T. Su, Y.-C. Chang, Y.-H. Lin, J.-F. Yeh, W.-C. Chen, and W. Hsu, "Dual-awareness attention for few-shot object detection," *IEEE Transactions on Multimedia*, 2021.
- [26] H. Law and J. Deng, "Cornernet: Detecting objects as paired keypoints," in *ECCV*, 2018.
- [27] X. Zhou, J. Zhuo, and P. Krahenbuhl, "Bottom-up object detection by grouping extreme and center points," in *CVPR*, 2019.
- [28] Z. Dong, G. Li, Y. Liao, F. Wang, P. Ren, and C. Qian, "Centripetalnet: Pursuing high-quality keypoint pairs for object detection," in *CVPR*, 2020, pp. 10 519–10 528.
- [29] D. Lin *et al.*, "Contrastive class-specific encoding for few-shot object detection," in *ICME*, 2022.
- [30] Q. Liao, X. Wang, B. Kong, S. Lyu, B. Zhu, Y. Yin, Q. Song, and X. Wu, "Transferable adversarial examples for anchor free object detection," in *2021 IEEE International Conference on Multimedia and Expo (ICME)*. IEEE, 2021, pp. 1–6.
- [31] Q. Liao, X. Wang, B. Kong, S. Lyu, Y. Yin, Q. Song, and X. Wu, "Fast local attack: Generating local adversarial examples for object detectors," in *2020 International Joint Conference on Neural Networks (IJCNN)*. IEEE, 2020, pp. 1–8.
- [32] M. Everingham, S. A. Eslami, L. Van Gool, C. K. Williams, J. Winn, and A. Zisserman, "The pascal visual object classes challenge: A retrospective," *IJCV*, vol. 111, no. 1, 2015.
- [33] T.-Y. Lin, M. Maire, S. Belongie, J. Hays, P. Perona, D. Ramanan, P. Dollár, and C. L. Zitnick, "Microsoft coco: Common objects in context," in *ECCV*. Springer, 2014.
- [34] R. Girshick, J. Donahue, T. Darrell, and J. Malik, "Rich feature hierarchies for accurate object detection and semantic segmentation," in *Proceedings of the IEEE conference on computer vision and pattern recognition*, 2014, pp. 580–587.
- [35] A. Neubeck and L. Van Gool, "Efficient non-maximum suppression," in *ICPR*, 2006.
- [36] A. Madry, A. Makelov, and et al., "Towards deep learning models resistant to adversarial attacks," in *ICLR*, 2018.
- [37] I. J. Goodfellow, J. Shlens, and C. Szegedy, "Explaining and harnessing adversarial examples," in *ICLR*, 2015.
- [38] B. Zhou *et al.*, "Learning deep features for discriminative localization," in *CVPR*, 2016, pp. 2921–2929.
- [39] R. R. Selvaraju *et al.*, "Grad-cam: Visual explanations from deep networks via gradient-based localization," in *ICCV*, 2017, pp. 618–626.
- [40] S. Liu, L. Qi, H. Qin, J. Shi, and J. Jia, "Path aggregation network for instance segmentation," in *Proceedings of the IEEE conference on computer vision and pattern recognition*, 2018, pp. 8759–8768.
- [41] G. Huang, Z. Liu, L. Van Der Maaten, and K. Q. Weinberger, "Densely connected convolutional networks," in *Proceedings of the IEEE conference on computer vision and pattern recognition*, 2017, pp. 4700–4708.
- [42] Z. Li and F. Zhou, "Fssd: feature fusion single shot multibox detector," *arXiv preprint arXiv:1712.00960*, 2017.
- [43] K. He, X. Zhang, S. Ren, and J. Sun, "Deep residual learning for image recognition," in *CVPR*, 2016.
- [44] F. Yu, D. Wang, E. Shelhamer, and T. Darrell, "Deep layer aggregation," in *CVPR*, 2018.
- [45] A. Newell, K. Yang, and J. Deng, "Stacked hourglass networks for human pose estimation," in *ECCV*. Springer, 2016.
- [46] G. K. Dziugaite, Z. Ghahramani, and D. M. Roy, "A study of the effect of jpg compression on adversarial images," *arXiv preprint arXiv:1608.00853*, 2016.
- [47] K. Simonyan and A. Zisserman, "Very deep convolutional networks for large-scale image recognition," *ICLR*, 2014.
- [48] N. Jain *et al.*, "On the robustness of human pose estimation," in *CVPR Workshops*, 2019, pp. 29–38.



Yunxu Xie is currently a postgraduate at the School of Computer Science, Chengdu University of Information Technology. His research directions are adversarial attack, deep learning, and computer vision.



Dr. Shu Hu is a Postdoc at Carnegie Mellon University. He received his Ph.D. degree in Computer Science and Engineering from University at Buffalo, the State University of New York (SUNY) in 2022. He received his M.A. degree in Mathematics from University at Albany, SUNY in 2020, and M.Eng. degree in Software Engineering from University of Science and Technology of China in 2016. His research interests include machine learning, digital media forensics, and computer vision.



Dr. Xin Wang (SM'2020) is a research affiliate at University at Buffalo, State University of New York. He received his Ph.D. degree in Computer Science from the University at Albany, State University of New York in 2015. His research interests are in machine learning, reinforcement learning, deep learning, and their applications. He is a senior member of IEEE.



Quanyu Liao is a graduate student at the School of Computer Science, Chengdu University of Information Technology. His research directions are adversarial attack, deep learning, and computer vision.



Bin B. Zhu received the B.S. degree in physics from the University of Science and Technology of China, Hefei, China, in 1986, and the M.S. and Ph. D. degrees in electrical engineering from the University of Minnesota, Minneapolis, MN, in 1993 and 1998, respectively. He is currently a Principal Researcher with Microsoft Research Asia, Beijing, China. His research interests include DNN security and privacy, AI applications, Internet and system security, privacy-preserving processing, content protection, and signal and multimedia processing.



Dr. Xi Wu is currently the dean of the School of Computer Science, Chengdu University of Information Technology, and the Chinese director of the International Joint Research Center for Image and Vision, Chengdu University of Information Technology. The main research directions are: image analysis and computational imaging, high-performance and parallel distributed computing, smart meteorology and numerical weather computing.



Dr. Siwei Lyu is an SUNY Empire Innovation Professor at the Department of Computer Science and Engineering, the Director of UB Media Forensic Lab (UB MDFL), and the founding Co-Director of Center for Information Integrity (CII) of University at Buffalo, State University of New York. Dr. Lyu received his Ph.D. degree in Computer Science from Dartmouth College in 2005, and his M.S. degree in Computer Science in 2000 and B.S. degree in Information Science in 1997, both from Peking University, China. Dr. Lyu's research interests include digital media forensics, computer vision, and machine learning. Dr. Lyu is a Fellow of IEEE.